Modeling of Soft Robots Actuated by Twisted-and-Coiled Actuators

Benjamin Pawlowski, Jiefeng Sun, Jing Xu, *Member, IEEE*, Yingxiang Liu, *Senior Member, IEEE*, and Jianguo Zhao, *Member, IEEE*

***Abstract*—Soft robots made from soft materials outperform traditional rigid robots in safety, maneuverability, and adaptability. Various methods have been proposed to actuate soft robots such as cables, pneumatic, or smart materials (e.g., shape memory alloys, dielectric elastomer, or ionic polymer-metal composites, etc.). In this paper, we propose to leverage a recently discovered artificial muscle—twisted-and-coiled actuators (TCAs)—to actuate soft robots. Compared with existing actuation methods, TCAs can be actuated electronically, can be embedded inside soft materials to enable distributed actuation, and are easy and low-cost to manufacture. We establish a general modeling framework for TCAs and TCA-actuated soft robots, including a physics-based model for TCAs as well as both the forward and inverse kinetostatics for TCA-actuated soft robots, where a coupling between TCA actuation and deformation of soft robots exists. Extensive experiments are conducted to verify the proposed models. The presented work will not only lay a theoretical foundation for using TCAs to actuate soft robots but also enable wider application for TCA-actuated soft robots (e.g., manipulation or locomotion).**

I. Introduction

SOFT robots made from soft materials have been an active and expanding area of research recently because these robots can leverage the inherent softness to accomplish tasks (e.g., locomotion or manipulation) that cannot be achieved with traditional rigid robots [1]–[4]. For instance, soft manipulators are safer than conventional rigid ones for humans to interact with and be around [2], making them beneficial for applications in medical devices, industrial environments, or in more personal settings (e.g., home). Soft manipulators can also deal with uncertain or difficult environments as their compliance allows for more adaptive motion and deformation when contacting, grasping, or avoiding objects [2]. Due to their advantages, many manipulators resembling biological structures have been developed recently (e.g., elephant trunks [5] and octopus arms [6]–[9]).

For soft manipulators, or more generally soft robots, the actuation is critical as it should be inherently soft to enable the flexibility of the robots. Two major types of actuator are used: tendons/cables [6], [8], [10]–[12] and pneumatics [7], [9], [13], [14]. Both types are simple to implement, can generate large motion, and are inherently compliant. The drawbacks for both actuation strategies are that they require bulky rigid components to function. For instance, the cables need motors to control the length for actuation, while pneumatics require a compressor and valves, all of which can take up substantial space, add weight, and decrease flexibility. Therefore, it is desirable to use actuators that require less external components for their functionality.

To address this problem, artificial muscles have recently been leveraged for actuating soft robots. Three prominent types are shape memory alloys (SMAs), dielectric elastomer actuators (DEAs), and ionic polymer-metal composites (IPMCs). SMAs can generate large actuations and forces, but have significant hysteresis and slow actuation rates [15], [16]. DEAs can actuate fast and accurately, but they require extremely high voltages and generate small forces [17]–[19]. IPMCs can generate large bending motion, but have large hysteresis and limited force generation [20], [21].

Besides existing artificial muscles, a recently discovered muscle, twisted-and-coiled actuator (TCA) [22], provides another viable actuation for soft robots. A TCA can actuate linearly if its temperature increases because of the thermal expansion and its twisted and coiled structure. TCAs can be conveniently fabricated from low-cost and commercially available polymer fibers (e.g., fishing lines, sewing threads) [22]. To fabricate a TCA, polymer threads are twisted together, and then the twisted threads are coiled into a helix, which is finally annealed to maintain the configuration. In general, TCAs are capable of producing 2.48 kJ/kg of specific work (∼50 times that of human muscle) and can provide 30% reversible stroke [23].

TCAs have two major advantages over typical actuation strategies (e.g., cables and pneumatics). First, they can be actuated electronically through Joule/resistive heating, can be embedded inside soft materials to enable distributed actuation, and are easy and low-cost to manufacture. Therefore, they are cost-effective actuators and will not need bulky components

Manuscript received January 29, 2018; revised June 27, 2018; accepted September 14, 2018. Date of publication October 1, 2018; date of current version February 14, 2019. Recommended by Technical Editor F. Iida. This work was supported in part by the National Science Foundation under Grant IIS 1755766 and by the National Natural Science Foundation of China under Grant 91748108. *(Corresponding author: Jianguo Zhao.)*

B. Pawlowski, J. Sun, and J. Zhao are with the Department of Mechanical Engineering, Colorado State University, Fort Collins, CO 80523 USA (e-mail: ben.pawlowski@comcast.net; J.Sun@colostate.edu; Jianguo.Zhao@colostate.edu).

J. Xu is with the Department of Mechanical Engineering, Tsinghua University, Beijing 100084, China (e-mail: jingxu@tsinghua.edu.cn).

Y. Liu is with the State Key Laboratory of Robotics and System, Harbin Institute of Technology, Harbin 150001, China (e-mail: liuyingxiang868@hit.edu.cn).

Color versions of one or more of the figures in this paper are available online at http://ieeexplore.ieee.org.

Digital Object Identifier 10.1109/TMECH.2018.2873014

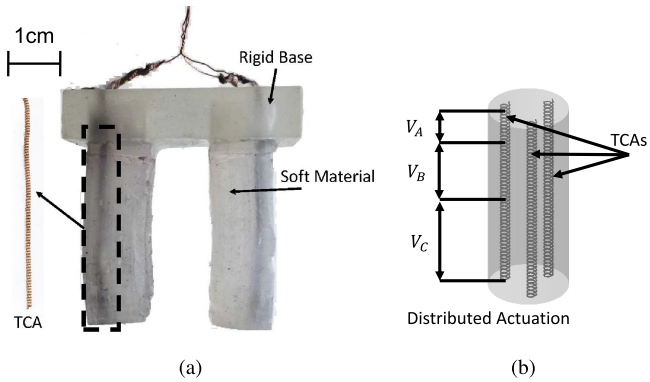

Fig. 1. (a) Soft gripper prototype used in our application for grasping in Section V-D. (b) Illustrative example of a soft manipulator using multiple TCAs and voltages to enable versatile 3-D motion.

to actuate a soft robot. Second, TCAs can sense their own deformations through the change of their electrical resistance, allowing for feedback of the geometry with simple current sensors [24], [25]. TCAs also have distinctive advantages compared with the most relevant actuator—coiled actuators made from SMA wires called SMA coils [26]. In particular, TCAs can be fabricated to contract or extend, while SMA coils can only contract, which requires prestretch for actuation, unnecessarily making the host soft structure stiffer [22].

Owing to the advantages of TCAs, we have recently investigated soft robots actuated by TCAs [27]. Fig. 1(a) depicts a TCA-actuated soft gripper with two soft fingers, each of them actuated by an extension TCA placed at the side of the finger. Although currently soft robots with only one TCA are demonstrated with bending, we can embed multiple TCAs at specific spatial locations inside soft materials to enable three-dimensional (3-D) motion. An illustrative example with three TCAs placed in parallel inside a soft cylinder is shown in Fig. 1(b). Further, since TCAs can be driven by electricity, we can apply different voltages to different segments of each TCA [e.g., the leftmost TCA in Fig. 1(b)] to enable distributed actuation, which can be leveraged for biologically inspired robot locomotion such as crawling, walking, or swimming.

Enabling TCA-actuated soft robots requires a modeling framework to relate the deformation of soft body and the actuation from TCAs. Such a framework, however, faces two challenges. First, mathematical models for TCAs are currently underexplored. Most of existing models rely on system identifications, which require extensive experiments and the results are only valid for a specific TCA [28]–[30]. Since TCAs' performances vary with fabrication conditions [22], it is critical to establish a general model for any TCA. Second, for TCA-actuated soft robots, we cannot separate the modeling for the body deformation from the actuation of TCAs since the deformation is coupled with actuation, which is uncommon and, to the best of our knowledge, is not discussed before.

There are three main contributions for this paper to address the previous challenges. First, TCAs have been adopted for many traditional robotic applications, e.g., robotic hand, orthosis, etc. [28], [31]–[33], but directly leveraging TCAs for soft robots is underexplored. Some preliminary research investigates soft skin [34] with contraction TCAs. In this paper, we show that extension TCAs are promising to actuate soft robots as they eliminate the required prestretch for contraction TCAs. Second, we establish a physics-based model for extension TCAs based on our previous research on contraction TCAs [35] so that the models can be applied to any TCA if the physical parameters (e.g., length, diameter, Young's modulus, etc.) are given. Compared with existing models, the proposed models will be general enough to model TCAs for other applications. Third, with the developed model for TCAs, we establish kinetostatics (both forward and inverse) models to capture the coupling between TCAs and soft bodies for TCA-actuated soft robots. Since the coupling exists for any embedded actuator, such a model can be applied to other soft manipulators with couplings.

The rest of this paper is organized as follows. In Section II, we discuss the model of contraction TCAs developed in our previous work [35] and adjust it to accommodate extension TCAs. In Section III, we develop the general forward kinetostatic model for soft robots with embedded artificial muscles and demonstrate the model with TCA actuation. In Section IV, we discuss a numerical method for the inverse kinetostatics, which uses the forward model to approximate the local inverse, making it more computationally efficient than direct inverse computations. In Section V, we validate the proposed models by comparing experimental results with simulation results. We also apply the proposed models to calculate the required temperature to successfully grasp objects using a TCA-actuated soft gripper.

II. Modeling of Extension TCAs

In order to model TCA-actuated soft robots, we first establish a physics-based model for TCAs, which is currently only available through system identifications. We have already developed a model for contraction TCAs and experimentally verified it [35]. In this paper, we will modify the model for extension TCAs, which are more effective in actuating soft robots since they do not require prestretch. For contraction TCAs, we need to prestretch them to generate an initial tension for actuation. The pretension causes the body to immediately be deformed if a single contraction TCA is embedded into soft material. Although we can choose stiffer body material to limit the deformation, then the TCA needs to generate a larger force to bend the body. We can also place a pair of contraction TCAs antagonistically to cancel out the pretension. In this case, however, one TCA also needs to generate a larger force to overcome the pretension from the other TCA to bend the body. Without prestretch, extension TCAs can bend a softer body with a smaller force, making them more effective in actuating soft robots.

Before introducing the models, we briefly describe the fabrication process to distinguish contraction and extension TCAs (detailed procedure in Section V-A). The fabrication process can be divided into three steps: twisting, coiling, and annealing [22], which are described as follows.

1) *Twisting:* One end of one or multiple polymer fiber threads (fishing line or sewing thread) is twisted by a DC motor, while the other end is constrained from rotation and an appropriate hanging weight is also attached to it to keep the fiber taut during the twisting process.

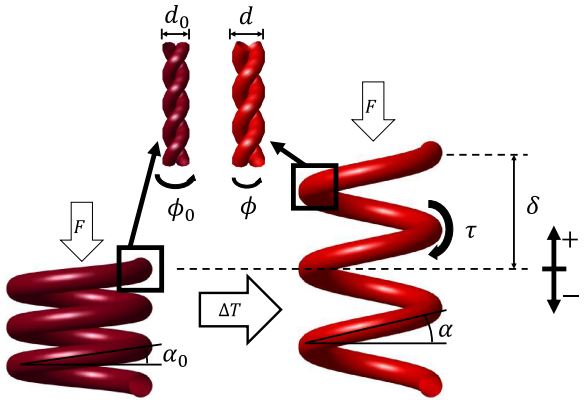

Fig. 2. Working principle of extension TCAs: They extend due to an internal untwisting torque, coming from the radial thermal expansion. The larger helices represent the coils of the TCAs and the smaller helices (two threads are used for an example) wrapped around each other represent the twisted threads inside the coil. The forces shown are applied and would be considered in the negative direction.

2) *Coiling:* After a critical amount of twists is inserted into the fiber, coils will start to form automatically along the fiber if the motor keeps rotating. Besides self-coiling, we can also coil the twisted fiber by wrapping it around a mandrel in the same or opposite direction of twisting. If the twisting and coiling directions are the same, then we will obtain a contraction TCA, or an extension TCA if they are opposite.
3) *Annealing:* After coils are formed, the twisted-and-coiled fiber is put into an oven to stabilize the structure so that it permanently attains the coiled configuration after being taken out of the oven. Eventually, we can obtain either contraction or extension TCAs.

The working principle for TCAs can be illustrated in Fig. 2 with extension TCAs as an example. With an extension TCA shown in the left-hand side of Fig. 2 subject to an external force, if the TCA's temperature is increased, the twisted fiber will tend to untwist due to radial thermal expansions, generating an untwisting torque acting along the cross section of the fiber. We do not consider the axial thermal expansion as the materials typically used for TCAs have a much smaller axial expansion (∼4% [22]) relative to their radial expansion. Such untwisting torques will push the coils apart to generate the extension motion due to the coiled structure of the TCA (right of Fig. 2). For contraction TCAs, the temperature-induced untwisting torque will be in the opposite direction, pulling the coils together for contraction. All these allow for the TCA to generate an axial force and deformation when a heat source is applied. If electrically conductive fibers are used, then the temperature can be increased via Joule heating of the TCAs.

The physics-based model will establish the relationship between the temperature, the applied force, and the displacement of a given TCA. First, the untwisting torque in the twisted fiber resulted from an increase of temperature can be obtained as [35]

$$\tau = \frac{G_T J_T \phi_0 (1 - d_0/d)}{l} \tag{1}$$

where G_T is the shear modulus, l is the length, and J_T is the polar second moment of area of the twisted fiber. ϕ is the number of twists of the fiber, d is the outer diameter of the twisted fiber, and the 0 subscript denotes the initial value. d can be obtained from d_0 through the coefficient of thermal expansion ρ: $d = d_0(1 + \rho\Delta T)$, where ΔT is the change in the temperature from the reference value.

With the untwisting torque, we can establish the relationship between the applied force, the displacement, and the torque using Castigliano's Second Theorem [35]. For this, the only torque is the internally generated one and the force is from an axial load at the end of the TCA. The resulting equation is

$$\delta = f_{11} F + f_{12} \tau \tag{2}$$

where δ is the linear displacement of the TCA, F is the applied force, and f_{11} and f_{12} are coefficients derived from Castigliano's Second Theorem [35] and are based on both the geometry and the material properties of the fiber used in the TCA. A positive δ corresponds to an increase in length and a positive F acts in the direction of extension. The specific forms of f_{11} and f_{12} are

$$f_{11} = \frac{8n}{\pi^3 d^4}\left(\frac{l}{n}\right)^3\left(\frac{\cos^4\alpha}{G_T} + \frac{2\sin^2\alpha\cos^2\alpha}{E_T}\right) + \frac{8n}{\pi d^2}\left(\frac{l}{n}\right)\left(\frac{\cos^2\alpha}{2G_T} + \frac{\sin^2\alpha}{2E_T}\right) \tag{3}$$

$$f_{12} = \frac{8n}{\pi^2 d^4}\left(\frac{l}{n}\right)^2 \frac{\cos^2\alpha}{G_T} \tag{4}$$

where E_T is the elastic modulus of the twisted fiber, n is the number of coils, and α the pitch angle of the TCA. All the parameters in (3) and (4) are known physical parameters for TCA except α. But α is a function of the displacement δ through the following geometric relationship:

$$\delta = l(\sin\alpha - \sin\alpha_0) \tag{5}$$

where α_0 is the initial pitch angle (see Fig. 2). Therefore, given any two parameters from δ, τ, and F, we can solve the other parameter through (2).

To integrate the TCA model in (2) with the model of TCA-actuated soft robots in the following section, we rewrite the force exerted by a TCA in a vector form

$$\boldsymbol{F} = \frac{\delta - f_{12}\tau}{f_{11}} \boldsymbol{t}_a \tag{6}$$

to include the force's direction using $\boldsymbol{t}_a$ as the unit vector tangent to the TCA. Here, we assume that the force generated by a TCA acts purely axially, which is reasonable due to TCAs being radially symmetric and causing all the torque to result in forces in the same direction. Equation (6) will be used later for the model of TCA-actuated soft robots.

We can derive the variables used in the modeling from measurable parameters of a TCA: the twisted fiber length, l, the final coiled length, L, the outer diameter of the TCA, D, and the number of twists, N. To convert these to variables in the model, we use the following geometric relationships: $\alpha_0 = a\sin(L/l)$, $n = 2\cos(\alpha_0)l/(\pi D)$, $\phi_0 = 2\pi N$, and $d_0 = 2DL/l$ [22]. The

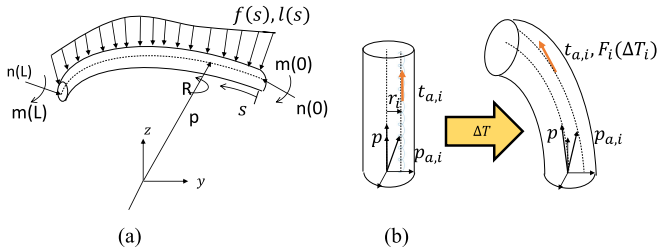

Fig. 3. Conceptual models for a TCA-actuated soft robot. (a) Diagram for a Cosserat Rod. $\boldsymbol{p}$ and R describe the position and rotation of the centerline from the fixed frame. $\boldsymbol{n}$ and $\boldsymbol{m}$ represent the internal force and moment, while $\boldsymbol{f}$ and $\boldsymbol{l}$ are the distributed force and moment, respectively. s is the distance along the centerline from the base and varies from 0 at the base to L at the tip. (b) Schematic for the modeling of TCA-actuated soft robot. A TCA extends if its temperature increases, deforming the robot from the reference configuration.

d_0 equation assumes that the TCA is fully compressed (the coils contact each other) before actuation.

The material properties of the polymer thread we used have been observed to change with temperature [30], [36]. We consider the relationships to be linear and use the values from [30] for ρ and E_T (we change the polynomial fit for E_T to a linear one).

III. Forward Kinetostatics of TCA-Actuated Soft Robots

Based on the modeling of TCA, we can establish models for TCA-actuated soft robots. As our first step, we aim to establish the kinetostatic model, which will serve as a basis for dynamics modeling in the future. Since TCAs are driven by temperature change, the forward kinetostatic problem for a TCA-actuated soft robot is to determine the robot's shape given the temperature for each of the embedded TCAs. In this case, we assume that the robot body be slender and thus can be considered as a rod/beam. To model the kinetostatics of a soft robot with embedded actuators, we combine the model for the robot body and the actuation model. For the modeling of robot body, we will leverage the Cosserat Rod model [11] to formulate the kinematic equations to describe the positions and rotations as well as static equations to establish the relationship between internal forces and moments and the distributed forces and moments. The actuation model will be the TCA model presented in Section II.

First, equations from the Cosserat Rod [11] can be used to model a soft body: the transformation of the position [see (7)], the rotation of the centerline [see (8)], the internal and distributed force balance [see (9)], and the internal and distributed moment balance [see (10)]:

$$\dot{\boldsymbol{p}} = R\boldsymbol{\nu} \tag{7}$$

$$\dot{R} = R\widehat{\boldsymbol{\omega}} \tag{8}$$

$$\dot{\boldsymbol{n}} + \boldsymbol{f} = 0 \tag{9}$$

$$\dot{\boldsymbol{m}} + \dot{\boldsymbol{p}} \times \boldsymbol{n} + \boldsymbol{l} = 0 \tag{10}$$

where the operator $\dot{}$ is the derivative with respect to $s \in \mathbb{R}$, which is the distance along the centerline from the base and varies from 0 to L, with L the length of the centerline in the reference configuration [see Fig. 3(a)]. The centerline is the curve that passes through all the centroids of the cross sections making up the body. $\boldsymbol{p} \in \mathbb{R}^3$ is the position vector of the cross section relative to the fixed frame, $R \in \mathbb{R}^{3\times3}$ the rotation matrix from the body frame to the fixed frame, $\boldsymbol{\nu} \in \mathbb{R}^3$ the linear strain, $\boldsymbol{\omega} \in \mathbb{R}^3$ the angular strain, $\boldsymbol{n} \in \mathbb{R}^3$ the internal force, $\boldsymbol{f} \in \mathbb{R}^3$ the distributed force, $\boldsymbol{m} \in \mathbb{R}^3$ the internal moment, and $\boldsymbol{l} \in \mathbb{R}^3$ the distributed moment. The operator $\widehat{\cdot}$ is the transformation from $\mathbb{R}^3$ to $se(3)$. Another operator, $\check{\cdot}$, will also be used later to represent the transformation from $se(3)$ to $\mathbb{R}^3$. Both $\widehat{\cdot}$ and $\check{\cdot}$ can also represent the transformations between $SE(3)$ and $\mathbb{R}^6$ [37].

The internal force and moment, dependent on the material properties and the strains, can be written as

$$\boldsymbol{n} = RK_\nu(\boldsymbol{\nu} - \boldsymbol{\nu}^*) \tag{11}$$

$$\boldsymbol{m} = RK_\omega(\boldsymbol{\omega} - \boldsymbol{\omega}^*) \tag{12}$$

where $K_\nu \in \mathbb{R}^{3\times3}$ and $K_\omega \in \mathbb{R}^{3\times3}$ are the linear and angular stiffness, respectively. For a homogeneous material, $K_\nu = \text{diag}(G_B A, G_B A, E_B A)$ and $K_\omega = \text{diag}(E_B I, E_B I, G_B J_B)$ where E_B is the elastic modulus of the body, G_B is the shear modulus. A, I, J_B is the area, the second moment of inertia, and the polar second moment of inertia of the cross section, respectively. The values with *'s are the values in the initial or reference configuration. In the case of a straight rod, these values are $\boldsymbol{\nu}^* = [0, 0, 1]^T$ and $\boldsymbol{\omega}^* = [0, 0, 0]^T$.

The distributed force and moment come from the forces in the embedded actuators. For TCAs, we assume that all forces are exerted axially and that there is no resistance to moments. These assumptions allow TCAs to be modeled as strings, which means they only need to be modeled with the force equilibrium. Therefore, the force in a TCA is determined from (6). The only modification is to add an index, i, to the forces and other parameters to indicate the ith TCA when multiple TCAs are used. In this case, the force can be written as

$$\boldsymbol{F}_i = \frac{\delta_i - f_{12}(\delta_i, T_i)\tau(T_i)}{f_{11}(\delta_i, T_i)}\boldsymbol{t}_{a,i}. \tag{13}$$

The dependencies on the temperature, T_i, and the displacement, δ_i, are made explicit in (13) for emphasis. The dependence on δ_i is important as it indicates the coupling between the body deformation and TCAs' actuation.

With $\boldsymbol{F}_i$, the distributed force for a system with N actuators can be written using the force equilibrium as

$$\boldsymbol{f} = \boldsymbol{f}_e + \frac{d}{ds}\sum_{i=1}^{N}\boldsymbol{F}_i \tag{14}$$

where $\boldsymbol{f}_e$ is an external distributed force. An example of an external force is the gravitational force and can be represented as $\boldsymbol{f}_e = \psi A R \boldsymbol{g}$, where ψ is the density of the material, A the cross-sectional area, and $\boldsymbol{g}$ the gravitational acceleration vector.

The distributed moment can then be computed from the distributed forces and the distance from the centerline [see Fig. 3(b)]

$$\boldsymbol{l} = \boldsymbol{l}_e + \sum_{i=1}^{N}\left(\widehat{R\boldsymbol{r}_i}\right)\frac{d}{ds}\boldsymbol{F}_i \tag{15}$$

where $\boldsymbol{l}_e$ is an external distributed moment, $\boldsymbol{r}_i$ is the distance of the actuator from the centerline in the fixed frame, and the inclusion of R is to rotate it into the body frame.

It is then necessary to know the forms of $\boldsymbol{t}_{a,i}$ and δ_i to compute the derivatives in the distributed terms. Both of them will depend on the position of the actuator, $\boldsymbol{p}_{a,i}$:

$$\boldsymbol{p}_{a,i} = \boldsymbol{p} + R\boldsymbol{r}_i \tag{16}$$

$$\boldsymbol{t}_{a,i} = \frac{\dot{\boldsymbol{p}}_{a,i}}{\|\dot{\boldsymbol{p}}_{a,i}\|} \tag{17}$$

$$\delta_i(s) = \int_0^s \|\dot{\boldsymbol{p}}_{a,i}(u)\| du - L_i s \tag{18}$$

where L_i is the ratio of the actuator's length to the centerline's length in the reference configuration. In the case when the actuator is aligned with the centerline and the reference configuration is straight, we have $L_i = 1$. The inclusion of L_i will allow us to investigate more general cases when the actuators do not align with the centerline. The value for δ_i is obtained through the current arc length minus the original arc length of the actuator up to the current position of s.

The derivatives of $\boldsymbol{p}_{a,i}$, $\boldsymbol{t}_{a,i}$, and δ_i with respect to s can then be computed as

$$\dot{\boldsymbol{p}}_{a,i} = R\left(\boldsymbol{\nu} + \widehat{\boldsymbol{\omega}}\boldsymbol{r}_i + \dot{\boldsymbol{r}}_i\right) \tag{19}$$

$$\dot{\boldsymbol{t}}_{a,i} = -\frac{\hat{\dot{\boldsymbol{p}}}^2_{a,i}}{\|\dot{\boldsymbol{p}}_{a,i}\|^3}\ddot{\boldsymbol{p}}_{a,i} \tag{20}$$

$$\dot{\delta}_i = \|\dot{\boldsymbol{p}}_{a,i}\| - L_i. \tag{21}$$

With that, we can get a system of ordinary differential equations (ODEs) in a common form for Cosserat models with the state variables as $\boldsymbol{p}$, R, $\boldsymbol{\nu}$, and $\boldsymbol{\omega}$. However, due to coupling between the body deformation and actuator's displacement, the common form cannot be separated from δ_i. To address this problem, we can incorporate δ_i as a state variable into the system since a differential form of it exists [see (21)]. In this case, the new system of ODEs can be written as

$$\dot{\boldsymbol{p}} = R\boldsymbol{\nu} \tag{22}$$

$$\dot{R} = R\widehat{\boldsymbol{\omega}} \tag{23}$$

$$\dot{\delta}_i = \|\dot{\boldsymbol{p}}_{a,i}(s)\| - L_i \tag{24}$$

$$\begin{bmatrix} a & b \\ c & d \end{bmatrix}\begin{bmatrix} \dot{\boldsymbol{\nu}} \\ \dot{\boldsymbol{\omega}} \end{bmatrix} = \begin{bmatrix} e \\ f \end{bmatrix} \tag{25}$$

where a, b, c, d, e, and f come from manipulating the previously developed system of equations

$$a = RK_\nu - \sum F_i \frac{\hat{\dot{\boldsymbol{p}}}^2_{a,i}}{\|\dot{\boldsymbol{p}}_{a,i}\|^3} R \tag{26}$$

$$b = -\sum F_i \frac{\hat{\dot{\boldsymbol{p}}}^2_{a,i}}{\|\dot{\boldsymbol{p}}_{a,i}\|^3} (-R\widehat{\boldsymbol{r}}_i) \tag{27}$$

$$c = -\sum \widehat{R\boldsymbol{r}_i} F_i \frac{\hat{\dot{\boldsymbol{p}}}^2_{a,i}}{\|\dot{\boldsymbol{p}}_{a,i}\|^3} R \tag{28}$$

$$d = RK_\omega - \sum \widehat{R\boldsymbol{r}_i} F_i \frac{\hat{\dot{\boldsymbol{p}}}^2_{a,i}}{\|\dot{\boldsymbol{p}}_{a,i}\|^3} (-R\widehat{\boldsymbol{r}}_i) \tag{29}$$

$$\begin{aligned} e = {} & R(K_\nu\dot{\boldsymbol{\nu}}^* - (\widehat{\boldsymbol{\omega}}K_\nu + \dot{K}_\nu)(\boldsymbol{\nu} - \boldsymbol{\nu}^*)) - \boldsymbol{f}_e \\ & - \sum \left(-F_i \frac{\hat{\dot{\boldsymbol{p}}}^2_{a,i}}{\|\dot{\boldsymbol{p}}_{a,i}\|^3} R(\widehat{\boldsymbol{\omega}}(\boldsymbol{\nu} + \widehat{\boldsymbol{\omega}}\boldsymbol{r}_i + 2\dot{\boldsymbol{r}}_i) + \ddot{\boldsymbol{r}}_i) \right) \end{aligned} \tag{30}$$

$$\begin{aligned} f = {} & R(K_\omega\dot{\boldsymbol{\omega}}^* + \widehat{\boldsymbol{\nu}}K_\nu(\boldsymbol{\nu} - \boldsymbol{\nu}^*) - (\widehat{\boldsymbol{\omega}}K_\omega + \dot{K}_\omega)(\boldsymbol{\omega} - \boldsymbol{\omega}^*)) \\ & - \boldsymbol{l}_e + \sum \widehat{R\boldsymbol{r}_i} F_i \frac{\hat{\dot{\boldsymbol{p}}}^2_{a,i}}{\|\dot{\boldsymbol{p}}_{a,i}\|^3} R(\widehat{\boldsymbol{\omega}}(\boldsymbol{\nu} + \widehat{\boldsymbol{\omega}}\boldsymbol{r}_i + 2\dot{\boldsymbol{r}}_i) + \ddot{\boldsymbol{r}}_i)) \end{aligned} \tag{31}$$

Equations (22)–(25) form a system of ODEs with state variables: $\boldsymbol{p}$, R, $\boldsymbol{\nu}$, $\boldsymbol{\omega}$, and δ_i with ($i = 1, \ldots, N$). The equations are in a general form independent of the actual form of F_i so that they can be applied for any string-like actuator. The initial values of the system ($s = 0$) will be $\boldsymbol{p} = \boldsymbol{0}$, $R = I_{3\times3}$, and $\delta_i = 0$ most of the time. However, we cannot determine the value of the initial strains prior to solving the system. Therefore, to fully constrain the system, boundary values for the strains must be determined. The boundary values for the strains can be solved for at the tip; however, they are not trivial since the force varies with the state variables.

To solve the strains, we need to use the force and moment balance equations. The only place the force and moment equations can be solved is at the tip cross section due to moments accumulating over the body. Taking the force and moment balance at the tip (includes the TCA forces, the internal strain force, and an arbitrary external load) and rearranging, we get

$$\boldsymbol{\nu} = \boldsymbol{\nu}^* - K_\nu^{-1}\left(\boldsymbol{F}_e + \sum_{i=0}^{N} F_i \frac{\boldsymbol{\nu} + \widehat{\boldsymbol{\omega}}\boldsymbol{r}_i + \dot{\boldsymbol{r}}_i}{\|\boldsymbol{\nu} + \widehat{\boldsymbol{\omega}}\boldsymbol{r}_i + \dot{\boldsymbol{r}}_i\|}\right) \tag{32}$$

$$\boldsymbol{\omega} = \boldsymbol{\omega}^* - K_\omega^{-1}\left(\boldsymbol{M}_e + \sum_{i=0}^{N} \widehat{R\boldsymbol{r}_i} F_i \frac{\boldsymbol{\nu} + \widehat{\boldsymbol{\omega}}\boldsymbol{r}_i + \dot{\boldsymbol{r}}_i}{\|\boldsymbol{\nu} + \widehat{\boldsymbol{\omega}}\boldsymbol{r}_i + \dot{\boldsymbol{r}}_i\|}\right) \tag{33}$$

the value $\boldsymbol{F}_e$ and $\boldsymbol{M}_e$ are an external force and moment applied at the tip of the rod, respectively. For example, it is important to consider these tip forces in the case of grasping.

It can be seen that (32) and (33) cannot be solved analytically without simplifications. Also, F_i can depend on the final values for the state variables, which are unknown prior to solving the system. To address this problem, we can leverage a boundary value problem (BVP) solver to numerically solve a system of ODEs with some initial conditions and some final conditions. The simplest BVP solver is the shooting method, which combines an initial value problem (IVP) solver and a root finding method to solve the BVP. An IVP solver requires either all initial conditions or all final conditions to be specified to solve the system of ODEs. Using an initial guess at the unknown

initial conditions, the shooting method first solves the ODEs with the IVP solver, and then updates the guess using a root finding method if the final boundary conditions are not met.

Using the shooting method for BVP solver, we solve the forward kinetostatics as follows: guess the values for $\boldsymbol{\nu}(0)$ and $\boldsymbol{\omega}(0)$, use an IVP solver (e.g., fourth-order Runge–Kutta method) to solve the state variables for $s \in [0, L]$, check that there is a force balance at the tip and that the displacements match. If they do not match, update the guessed values and repeat the process until they do. The execution speed is roughly 0.05 s for the BVP solver and 0.001 s for the IVP solver when ran on a laptop with an i7-U4600 CPU with 8 GB of RAM. The proposed computation scheme is stable since the only times the solution will not converge is when intentionally bad initial guesses are provided.

IV. Inverse Kinetostatics of TCA-Actuated Soft Robots

In order to control a TCA-actuated soft robot, it is necessary to compute the required temperatures to achieve a desired configuration. Again, as our initial step, we ignore the dynamic effect. In this case, the problem is to solve the inverse kinetostatics of a TCA-actuated soft robot. A straightforward solution is to leverage forward kinetostatics to iteratively update the guess for the temperatures until the desired configuration is achieved (brute-force optimization); however, such a process is very time-consuming as running many iterations of the forward solver is inefficient. In this case, we will leverage a more efficient method of finite difference [38]. This method approximates the necessary change in actuation values to move toward a desired configuration by posing the forward kinetostatics as an IVP rather than a BVP, solving it several times to approximate the local inverse kinetostatics, which greatly speed up the computation.

Similar to [38], we first rearrange the forward kinetostatics equations to contain a description of the kinematics, g, a system of ODEs for state variables, $\boldsymbol{y}$, and a boundary condition, $\boldsymbol{b} = 0$

$$\dot{g} = g\hat{\boldsymbol{\xi}}(\boldsymbol{y}) \tag{34}$$

$$\dot{\boldsymbol{y}} = f(s, \boldsymbol{y}, g, \boldsymbol{q}, \boldsymbol{W}) \tag{35}$$

$$\boldsymbol{b}(\boldsymbol{y}(L), g(L), \boldsymbol{q}, \boldsymbol{W}) = \boldsymbol{0} \tag{36}$$

where $g = \left[\begin{smallmatrix} R & \boldsymbol{p} \\ \boldsymbol{0} & 1 \end{smallmatrix}\right]$ is the homogeneous transformation matrix describing the shape of the centerline curve, $\boldsymbol{\xi} = [\boldsymbol{\nu}, \boldsymbol{\omega}]^T$ is the strain vector, $\boldsymbol{q}$ are the actuation parameters (the changes in temperature), and $\boldsymbol{W}$ is the external wrench applied to the tip of the manipulator. The function $\boldsymbol{b}$ is comprised of the force (32) and moment (33) balance equations at the tip and the agreement of the guessed value and the computed value of δ_i in the solver.

Since we do not have all the initial conditions for the state variables, $\boldsymbol{y}$, we separate the initial conditions of the state variables into known, $\boldsymbol{y}_k(0)$, and unknown, $\boldsymbol{y}_u(0)$. The unknown initial conditions make it necessary to use the BVP solver discussed in the prior section. However, if we know the values for $\boldsymbol{y}_u(0)$, we could use a much more efficient IVP solver for the computation. Therefore, if we have a known solution for the unknown initial conditions, we can change the BVP to an IVP.

Changing the forward model from a BVP to an IVP via a known solution enables us to see how small perturbations in the initial conditions, actuation values, and tip wrench will influence the system. The results of small perturbations on the system can then allow us to approximate the inverse kinetostatics near the known solution used. Then, we may use repeated applications of the approximated inverse to converge to a desired configuration. How to construct the approximate inverse kinetostatics from the perturbations follows from [38] and is described in the rest of the section.

First, we describe how the shape of the robot changes in space and time (i.e., the strain and velocity along the centerline) using the following two equations [38]:

$$\dot{g} = g\hat{\boldsymbol{\xi}} \tag{37}$$

$$g' = g\hat{\boldsymbol{\eta}} \tag{38}$$

where $\boldsymbol{\eta}$ is the twist vector representing the linear and angular velocities. The operator $\cdot'$ represents the derivative with respect to time, and the operator $\dot{\cdot}$ still represents the derivative with respect to s.

Then, the twist vector can be written as [38]

$$\boldsymbol{\eta} = (g^{-1}g')^{\vee} = J\boldsymbol{q}' + C\boldsymbol{W}' \tag{39}$$

where J is the Jacobian associated with the change in actuation values, and C, called the compliance matrix, is the Jacobian associated with changes in the tip wrench.

Discretizing (39) can be leveraged to compute the inverse kinetostatics. After eliminating time terms from both sides, the discretization is

$$\Delta\boldsymbol{x} = J\Delta\boldsymbol{q} + C\Delta\boldsymbol{W} \tag{40}$$

where $\boldsymbol{x}$ is the configuration value we want to control (e.g., tip position).

The J and C matrices can then be written in terms of submatrices that can be computed via the IVP solver and the perturbations [38]:

$$J = E_q - E_u B_u^{-1} B_q \tag{41}$$

$$C = E_W - E_u B_u^{-1} B_W \tag{42}$$

where the E and B are submatrices obtained by differentiation $E_z = \frac{d(g^{-1}g)^{\vee}}{dz}$ and $B_z = \frac{d\boldsymbol{b}}{dz}$, where $z \in \{q, u, W\}$ represents the differentiation variable. These are the matrices approximated via the perturbation and IVP solutions.

Equations for J and C can be approximated with any method for approximating first derivatives (e.g., first-order forward finite differences). The approximations are specifically for the E and B matrices, which are then used to form J and C. With the approximations, the inverse kinetostatics can be iteratively approximated to reach a particular configuration.

We show that the finite difference approach is more computationally efficient by comparing its computation speed with the brute force optimization approach. Both codes use the same forward model for the computations. The finite difference

scheme converges roughly eight times faster than the optimization scheme. One iteration of the finite difference scheme runs the forward integration (IVP solver) $12 + 2N$ times with N the number of actuators, and one iteration of the BVP solver for the resulting configuration. Since most of the computations are with the forward model, the finite difference scheme can finish one computation in roughly $0.001(12 + 2N) + 0.05$ s.

The inverse kinetostatics can be applied to solve the required temperature for grasping objects with two TCA-actuated fingers, which will be experimentally verified in the next section. In this case, we can slightly modify the inverse kinetostatics by rewriting (40) using the simplification of $\Delta \boldsymbol{x} = 0$ to determine the required temperature

$$\Delta \boldsymbol{q} = -J^{-1} C \Delta \boldsymbol{W}. \tag{43}$$

This will allow us to incrementally determine the temperature necessary to exert a particular force for the manipulator.

V. Simulation and Experimental Results

We conduct a series of experiments to verify the proposed models. We first validate the model for extension TCAs by fixing the force applied to a TCA, varying the temperature, and recording the associated displacements. To validate both the forward and inverse kinetostatics, we leverage a soft manipulator actuated by a single TCA since this allows us to validate the simplest form of the proposed models. For forward kinetostatics, we increase the temperature applied to the TCA and obtain the resulting shape of the manipulator to compare with simulation results. For inverse kinetostatics, we fix the end of the soft manipulator and record the generated tip force when the temperature of TCA increases. Finally, we demonstrate an application in the form of a miniature gripper with two TCA-actuated fingers.

To demonstrate the advantages of physics-based modeling, we fabricate TCAs with different number of threads and soft manipulators with different cross sections. The material properties for the EcoFlex body will remain constant throughout the experiments. These properties are: $\psi = 1040$ kg/m^3, $E_B = 37.8$ kPa, and $\nu = 0.5$, which are found in or can be computed from [39]. The TCAs will all be constructed from Shieldex Trading silver coated nylon sewing threads with a diameter of 0.2 mm (235/35 4ply Silver Thread, PN# 260151023534oz). The TCA parameters are obtained from fabrication and will be detailed in specific discussions.

For the simulations, we always use the following initial conditions: $\boldsymbol{p} = \boldsymbol{0}$, $R = I_{3\times3}$, and $\delta_i = 0$. The tip boundary condition is as discussed before, defined by the tip force and moment balance [see (32) and (33)] and the condition that the guessed and computed δ_i equal each other. The initial guess is always the value for the reference configuration. We note that the initial guesses do not seem to influence the final answer unless the initial guess is intentionally poor.

A. Validating the Model for Extension TCAs

The model for extension TCAs establishes the relationship between temperature, applied force, and displacement. To validate the model, we choose to fix the applied force by attaching a weight to a TCA, then increasing the temperature and measuring the corresponding displacement.

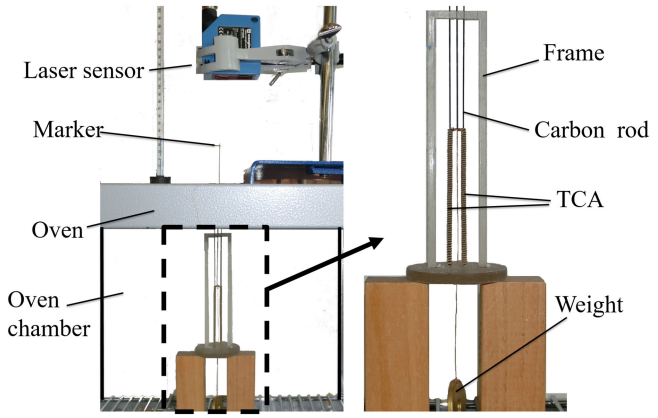

Fig. 4. Experimental setup for verifying models of extension TCAs. The detailed setup inside the dashed rectangle in the left figure is enlarged on the right.

For simulations, we predict the displacement δ using the TCA model given an attached weight and a temperature. To compute δ, we set (5) and (2) equal to each other. Then, the resulting equation, $l(\sin\alpha - \sin\alpha_0) = f_{11}F + f_{12}\tau$, is solved for α since all other parameters are known. Once α is computed, we can obtain the displacement, δ, which can then be compared with the experimental results.

The fabrication process of TCAs used in our experiments is similar to the method in [22]. The only difference is that the mandrel we used to coil the TCA is a taut copper wire instead of a rigid rod. The benefit of this is that we can decrease the spring index of TCAs by using wires with smaller diameters, and the wire does not need to be rigid. We twist three threads together by hanging a weight 600 g, and the process ends after inserting $N = 300$ rotations before self-coiling. From our experience, a weight heavier than 600 g may easily break the threads and a lighter weight will not allow for enough twisting of the threads. Two motors hold the two ends of a copper wire and keep it taut. Both motors rotate in the same direction to coil the twisted threads in heterochirality (i.e., coiling and twisting have opposite chirality) to generate an extension TCA [22]. The actuator is then annealed in an oven (Quincy Lab 10GCE, accuracy 0.5 °C) for 2 h at a temperature of 160 °C, and after that the actuator is stabilized and does not untwist when the copper wire is removed. The resulting TCA has the following parameters: $l = 110$ mm, $L = 497$ mm, $D = 2$ mm. To better verify the proposed model, we fabricated another TCA with four threads: $l = 110$ mm, $L = 471$ mm, $N = 259$ rotations, $D = 2.13$ mm.

In contrast to contraction TCAs, which can stay straight by contracting force when actuated [35], extension TCAs will buckle when actuated if no mechanism is used to constrain sideway movements. In this experiment (the setup is shown in Fig. 4), we fold the fabricated TCA into two segments (55 mm for each segment) that can cancel untwisting force with each other, and insert a rigid carbon rod into the TCA's center. A weight is hung at the middle of connection between two TCA

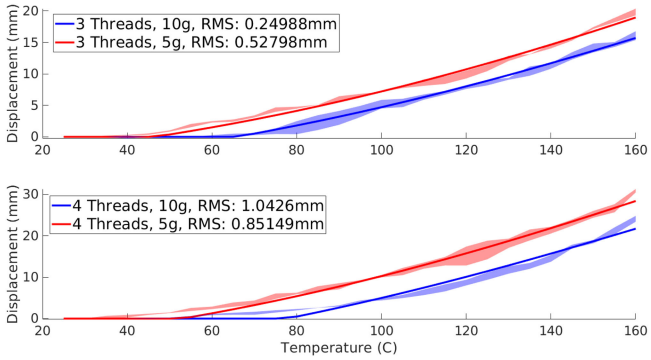

Fig. 5. Simulation versus experimental results for extension TCAs with three threads and four threads with different hanging weights. The shaded regions represent the experimental data (average ± standard deviation), and the rms values are derived from the simulation and the average experimental value.

segments to apply a constant force. The extending displacement, indicated by a marker raised out of the oven from a vent hole, is recorded by a laser displacement sensor (OPT2006, Wenglor sensoric GmbH) mounted at the top of the oven. A 3-D printed frame that can withstand high temperature keeps the carbon rods vertical to minimize errors. For each TCA (with three or four threads), we use two different weights: 5 and 10 g. For each TCA and weight, we conduct three experiments by increasing the temperature inside the oven with a step size of 5 °C, starting from 25 °C and ending at 160 °C.

The displacement of the TCA is plotted against the temperatures and compared with simulation results in Fig. 5. To quantify the error between the model and the experimental data, we report the root-mean-squared (rms) value between the averaged experimental results and the simulated results. This value quantifies the total error across the tested domain. A small value implies that the model is accurate across the entire test data, but larger values imply either a large error across the entire domain or over a small region. To locate the error, we plot a region within one standard deviation of the experimental data and the simulated data for a visual check. The comparisons for both forward and inverse kinetostatics are illustrated using the same approach in the next two sections.

From Fig. 5, the simulations have relatively low rms values and generally agree with experimental results. However, we note that there are some friction effects between TCAs and the guide rod during experiments. We compensate the friction by applying an additional equivalent hanging mass of 2.5 g for the 5 g case and 5 g for the 10 g case to the actuator and they are assumed constant throughout the experiment. The equivalent weights are approximated by first observing the relative angle of the thread connected to the hanging weight to the guide rod and using a friction coefficient to approximate the normal and friction forces. The most noticeable discrepancy is for the TCA with four threads, especially the point at which extension begins. This could be due to the friction not being properly accounted for (e.g., it varies with displacement or temperature), or when the TCA is fully compressed the threads will still expand due to changes in temperature and this expansion will cause small displacements upwards even though the coils still contact with each other. This effect is not modeled in our simulations and could lead to discrepancies at lower temperatures.

B. Validating the Forward Kinetostatics

To validate the forward kinetostatics for TCA-actuated soft robots, we fabricate soft manipulators with a single-embedded TCA but with two different cross section shapes: circular and square. With these two manipulators, we aim to compare the predicted bending shape with the experimental one for a given temperature of the TCA. All the TCAs used in the manipulator have the following parameters: $D = 1.7$ mm, $\alpha_0 = 15°$, and $N = 76.4$ rotations, the only difference is the TCA length L.

To quantify the shape for comparison, we assume that the soft manipulator will have a circular bending shape after the TCA is actuated. In this case, we use three sample points along the body for both experiments and simulations to calculate the radius for comparisons, as three points are the minimal number to determine a circle. The sample points are located at the base, the tip, and the center of the manipulator and are along the inner edge of the manipulator with respect to the bending direction. The radius can be obtained by fitting a circle to the three sampled points. Note that such a simplified quantification of the shape can make reasonable comparisons between simulations and experiments.

The soft manipulator with an embedded TCA is fabricated as follows. The TCA is fabricated using the same procedure for the TCAs in Section V-A. For the manipulator of a square cross section, EcoFlex10 is poured into a 3-D printed mold, in which a TCA is arranged in a U-shape, essentially acting like two parallel TCAs with the same temperature in order to generate enough force. After curing, the copper wires inside the TCA are pulled out and additional EcoFlex is used to seal the tip of the manipulator. The resulting manipulator has a side length of 10 mm and a usable length of 40 mm. Then, if we consider the two halves of the U-shaped TCA as separate TCAs, they both have lengths of $L = 40$ mm, and are located 3 mm from the neutral layer of the body. The fabrication procedure of the soft manipulator of a circular cross section is the same as above and the resulting manipulator has a diameter of 8 mm and a length of 40 mm. A single TCA is placed 3 mm from the center axis of the manipulator.

To perform the experiments, we embed a thermistor (EPCOS B57540G0503F000) close to the base of the TCA and fix the bottom of the body to a stand. Then, we place the manipulator inside the same oven for the TCA experiment, use the thermistor to measure the internal temperature, and position a camera outside the oven to capture an image of the manipulator through the oven's transparent door at increasing temperatures with a step size of 5 °C. Then, we calculate the radius for the inner edge of the body to quantify the manipulator's bending shape in each image, using the three sample points as discussed prior. In simulations, we derive the curvature in the same manner. The simulation is run at a given temperature and then the radius is calculated from the three sample points.

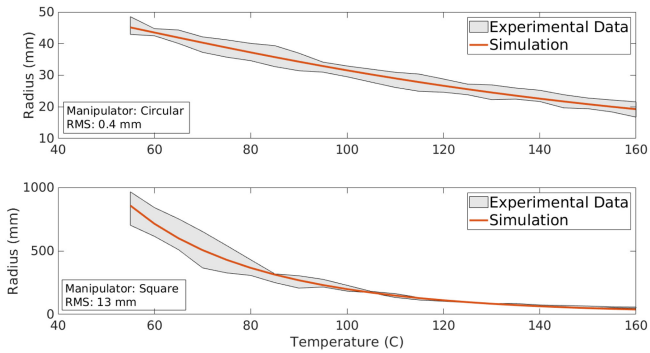

Fig. 6. Radius approximations comparing the prediction and the experimentally measured radii for a manipulator with a circular cross section (upper) and square cross section (lower). The gray region is the experimental average $\pm$ the standard deviation. RMS is computed from the simulation results and the average experimental results.

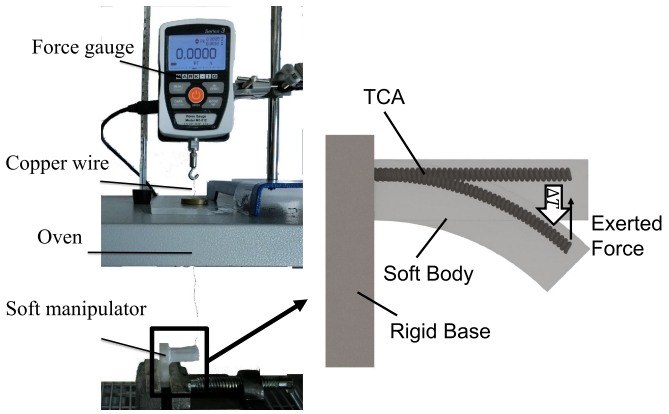

Fig. 7. Experimental setup for measuring the force exerted when the manipulator bends to a fixed position.

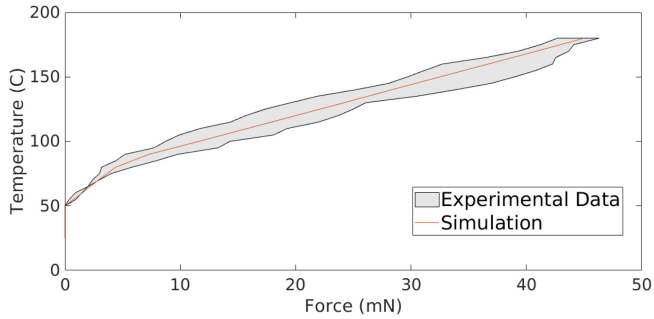

Fig. 8. Comparisons for the predicted and the experimental temperature. The rms value between the average experimental force and the predictions is 0.74 mN.

The comparisons between model prediction and experiments are plotted in Fig. 6. We note that the manipulator with a circular cross section has some initial bending while the square one does not. This causes the circular manipulator's curvature to be more linear and smaller at the beginning of the experiments. In the simulations, the initial bending is considered in the value for $\boldsymbol{\xi}^*$.

The predictions match the experimental results quite well. The exception being that the rms value is slightly high for the square cross section. This is likely due to the wide variance observed at the beginning of the experiments. Nevertheless, the simulation results fall well within the experimental range, indicating that it is still a reasonable fit.

C. Validating the Inverse Kinetostatics

To validate the inverse kinetostatics for TCA-actuated soft robots, we also use a soft manipulator actuated by a single extension TCA. Different from experiments for validating the forward kinetostatics, we fix the tip position of the manipulator, increase the temperature, and then measure the force generated at the tip of the manipulator. To do this in simulation, we run the finite difference approach discussed in Section IV to predict the required temperature from measured force [see (43)].

A similar fabrication approach is used to manufacture the soft manipulator with a square cross section actuated by a U-shaped TCA for this experiment. The fabricated manipulator has a side length of 10 mm and a usable length of 26 mm. If we consider the two halves of the U-shaped TCA as separate TCAs, their parameters are: $L = 26$ mm, $D = 1.7$ mm, and are located 3 mm from the center.

In this experiment, the soft manipulator is again placed inside the oven. One end of a flexible copper wire with a diameter of 0.1 mm is attached to the tip of the manipulator, while the other end connects to a force gauge (MARK-10-M3-012, Mark-10 Corporation) through a vent hole of the oven to measure force generated by the soft manipulator. The copper wire is loosely arranged to make sure the soft body can have a specific and fixed bending, after which the wire becomes taut and the generated forces can be measured by the force gauge. A thermistor, embedded in the soft manipulator touching the TCA, indicates the time when the TCA reaches the desired temperature. The temperature of the oven is controlled to increase the TCA's temperature by a step size of 5 °C from the room temperature. Fig. 7 shows the experimental setup with a detailed view where the initial state and the final state of the soft manipulator are overlapped.

Three experiments are conducted and the results are plotted in Fig. 8 to compare with the simulation results. During experiments, we observe an obvious extension of the soft manipulator due to a lack of a limiting layer. Also, from 25 °C to about 55 °C, the copper wire is still loose, and therefore no force is shown in the force gauge. Then, the force rises as the temperature increases. Some discrepancies exist between the individual experiments, which might be caused by the slightly different final locations for the manipulator's tip.

We can see from Fig. 8 that the simulation predictions match quite well with the experimental results. We note that there is a slight motion from 0–10 mN due to small deformations of the copper wire as it straightens out, and we incorporate this motion into the simulation.

D. Application: Grasping Objects

As an application of the proposed models, we fabricate a soft gripper with two fingers, each of which is actuated by one TCA. By controlling the temperature of TCA, we can tune contact

TABLE I
TEMPERATURES AT WHICH DIFFERENT WEIGHTS CAN BE GRASPED AND LIFTED USING A GRIPPER WITH TWO TCA-ACTUATED FINGERS

Grasping Weight	1 g	2 g	3 g
Firm grip temperature (°C)	95	120	135
Simulation Prediction (°C)	93.7	114.8	136.3

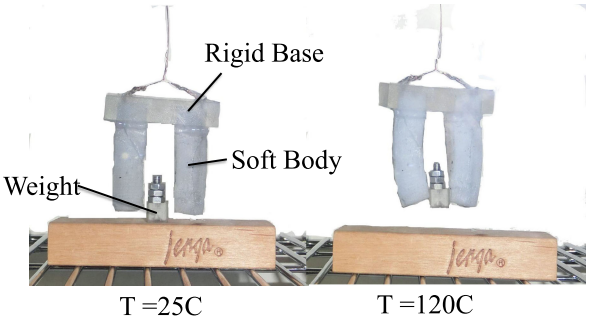

Fig. 9. Example of the grasper picking up an object.

forces applied onto an object to grasp and lift different objects with the same size but different weights. In this experiment, we demonstrate that the developed model can predict the required temperature to generate sufficient forces for grasping.

The fabrication process for the gripper is as follows. First, two soft fingers with a length of 20 mm and the same size of the cross section for the manipulator used in Section V-C are fabricated separately. Then, these two fingers are connected together on a 3-D printed rigid base with extra EcoFlex 10. Three different weights (1, 2, and 3 g) are used to test the required temperatures for successful grasping.

Given a weight of an object, the minimum required grasping force is determined through

$$\mu n F(T) = mg \tag{44}$$

where μ is the friction coefficient between the finger and the weight, n is the number of fingers, and m is mass of the weight. In order to keep μ the same, the size and the outer material of the weights (VeroClear RGD810 printing material) that contact with the gripper are kept the same and the mass of weight is changed by adding metal nuts and screws. The value of $\mu = 1.1$ is experimentally obtained by dragging the RGD810 material on the surface of Ecoflex 10 and measuring the drag force.

With the minimum required force, we calculate the required temperature for grasping using the inverse kinetostatic model. To experimentally obtain the required temperature, we place the whole system inside the oven and increase the oven's temperature with a step size of 5 °C. At each temperature, we pull the wire attached to the gripper to see if the weight can be lifted up. The required temperature is recorded if the weight can be lifted up for at least ten trials, and we term this temperature as a "firm grip" (see Table I). An example of grasping can be seen in Fig. 9.

Table I shows the firm grip temperatures and the predicted values using simulations. The results suggest the predictions are in rough correspondence with the experimental results. Discrepancies may come from the relative large step size of temperature: 5 °C. Also, the value of the friction coefficient, μ, might be influenced by temperature. Finally, the fingers bend slightly asymmetrical during experiments, leading to discrepancies as the simulation assumes them being identical.

VI. CONCLUSION

TCA is a newly discovered artificial muscle. With its unique characteristics (e.g., low-cost, easy-to-fabricate, and can generate extension motion) compared with existing actuation methods, it is a promising candidate for actuating soft robots. In this paper, we establish a modeling framework for TCA-actuated soft robots and experimentally verify the proposed models. The models include a physics-based model for TCAs and the kinetostatic model for TCA-actuated soft robots. The physics-based model can be leveraged for predicating the motion of any TCA if the physical parameters are given, while the kinetostatic model is general enough to describe the kinetostatics for soft robots with embedded actuations when coupling exists between the actuation and body deformation. Experimental results in general match with the modeling results, with some discrepancy that may come from the imperfection of experiments, imprecise value for some physical parameters, or nonideal way of quantifying the results. The developed model can lay a foundation for the application of TCAs in or beyond soft robots.

REFERENCES

[1] D. Trivedi, C. D. Rahn, W. M. Kier, and I. D. Walker, "Soft robotics: Biological inspiration, state of the art, and future research, " *Appl. Bionics Biomech.*, vol. 5, no. 3, pp. 99–117, 2008.
[2] D. Rus and M. T. Tolley, "Design, fabrication and control of soft robots, " *Nature*, vol. 521, no. 7553, pp. 467–475, 2015.
[3] S. Kim, C. Laschi, and B. Trimmer, "Soft robotics: A bioinspired evolution in robotics, " *Trends Biotechnol.*, vol. 31, no. 5, pp. 287–294, 2013.
[4] C. Laschi and M. Cianchetti, "Soft robotics: New perspectives for robot bodyware and control," *Frontiers Bioeng. Biotechnol.*, vol. 2, 2014. [Online]. Available: https://www.frontiersin.org/article/10.3389/fbioe.2014.00003
[5] S. Neppalli, M. A. Csencsits, B. A. Jones, and I. D. Walker, "Closed-form inverse kinematics for continuum manipulators, " *Adv. Robot.*, vol. 23, no. 15, pp. 2077–2091, 2009.
[6] M. Giorelli, F. Renda, G. Ferri, and C. Laschi, "A feed-forward neural network learning the inverse kinetics of a soft cable-driven manipulator moving in three-dimensional space," in *Proc. IEEE/RSJ Int. Conf. Intell. Robots Syst.*, Nov. 2013, pp. 5033–5039.
[7] D. Trivedi, A. Lotfi, and C. D. Rahn, "Geometrically exact models for soft robotic manipulators," *IEEE Trans. Robot.*, vol. 24, no. 4, pp. 773–780, Aug. 2008.
[8] M. Giorelli, F. Renda, M. Calisti, A. Arienti, G. Ferri, and C. Laschi, "A two dimensional inverse kinetics model of a cable driven manipulator inspired by the octopus arm," in *Proc. IEEE Int. Conf. Robot. Autom.*, May 2012, pp. 3819–3824.
[9] W. McMahan, B. Jones, I. Walker, V. Chitrakaran, A. Seshadri, and D. Dawson, "Robotic manipulators inspired by cephalopod limbs," in *Proc. Canadian Eng. Educ. Assoc.*, 2011, pp. 1–10.
[10] D. B. Camarillo, C. R. Carlson, and J. K. Salisbury, "Configuration tracking for continuum manipulators with coupled tendon drive," *IEEE Trans. Robot.*, vol. 25, no. 4, pp. 798–808, Aug. 2009.
[11] D. C. Rucker and R. J. W. III, "Statics and dynamics of continuum robots with general tendon routing and external loading," *IEEE Trans. Robot.*, vol. 27, no. 6, pp. 1033–1044, Dec. 2011.
[12] F. Renda, M. Cianchetti, M. Giorelli, A. Arienti, and C. Laschi, "A 3D steady-state model of a tendon-driven continuum soft manipulator inspired by the octopus arm," *Bioinspiration Biomimetics*, vol. 7, no. 2, 2012, Art. no. 025006.
[13] M. Rolf and J. J. Steil, "Efficient exploratory learning of inverse kinematics on a bionic elephant trunk," *IEEE Trans. Neural Netw. Learn. Syst.*, vol. 25, no. 6, pp. 1147–1160, Jun. 2014.

[14] B. A. Jones and I. D. Walker, "Kinematics for multisection continuum robots," *IEEE Trans. Robot.*, vol. 22, no. 1, pp. 43–55, Feb. 2006.
[15] S. Seok, C. D. Onal, K. J. Cho, R. J. Wood, D. Rus, and S. Kim, "Meshworm: A peristaltic soft robot with antagonistic nickel titanium coil actuators," *IEEE/ASME Trans. Mechatronics*, vol. 18, no. 5, pp. 1485–1497, Oct. 2013.
[16] H.-T. Lin, G. G. Leisk, and B. Trimmer, "Goqbot: A caterpillar-inspired soft-bodied rolling robot," *Bioinspiration Biomimetics*, vol. 6, no. 2, 2011, Art. no. 026007.
[17] J. Shintake, S. Rosset, B. E. Schubert, D. Floreano, and H. R. Shea, "A foldable antagonistic actuator," *IEEE/ASME Trans. Mechatronics*, vol. 20, no. 5, pp. 1997–2008, Oct. 2015.
[18] E. Acome *et al.*, "Hydraulically amplified self-healing electrostatic actuators with muscle-like performance, " *Science*, vol. 359, no. 6371, pp. 61–65, 2018.
[19] K. Jung *et al.*, "Artificial annelid robot driven by soft actuators," *Bioinspiration Biomimetics*, vol. 2, no. 2, 2007, Art. no. S42.
[20] M. Shahinpoor, Y. Bar-Cohen, J. Simpson, and J. Smith, "Ionic polymer-metal composites (IPMCs) as biomimetic sensors, actuators and artificial muscles-A review," *Smart Mater. Struct.*, vol. 7, no. 6, 1998, Art. no. R15.
[21] S.-W. Yeom and I.-K. Oh, "A biomimetic jellyfish robot based on ionic polymer metal composite actuators," *Smart Mater. Struct.*, vol. 18, no. 8, 2009, Art. no. 085002.
[22] C. S. Haines *et al.*, "Artificial muscles from fishing line and sewing thread," *Science*, vol. 343, no. 6173, pp. 868–872, 2014.
[23] C. S. Haines, N. Li, G. M. Spinks, A. E. Aliev, J. Di, and R. H. Baughman, "New twist on artificial muscles," *Proc. Nat. Acad. Sci.*, vol. 113, pp. 11709–11716, 2016.
[24] J. Zhao and A. Abbas, "A low-cost soft coiled sensor for soft robots," in *Proc. ASME Dyn. Syst. Control Conf.*, 2016, pp. V002T26A006–V002T26A006.
[25] J. van der Weijde, B. Smit, M. Fritschi, C. van de Kamp, and H. Vallery, "Self-sensing of deflection, force, and temperature for joule-heated twisted and coiled polymer muscles via electrical impedance," *IEEE/ASME Trans. Mechatronics*, vol. 22, no. 3, pp. 1268–1275, Jun. 2017.
[26] B. Holschuh, E. Obropta, and D. Newman, "Low spring index NiTi coil actuators for use in active compression garments," *IEEE/ASME Trans. Mechatronics*, vol. 20, no. 3, pp. 1264–1277, Jun. 2015.
[27] Miniature soft bending actuator with embedded coiled muscles, 2016. [Online]. Available: https://softroboticstoolkit.com/book/miniature-soft-bending-actuator-embedded-coiled-muscles
[28] M. C. Yip and G. Niemeyer, "High-performance robotic muscles from conductive nylon sewing thread," in *Proc. IEEE Int. Conf. Robot. Autom.*, Seattle, WA, USA, 2015, pp. 2313–2318.
[29] M. C. Yip and G. Niemeyer, "On the control and properties of supercoiled polymer artificial muscles," *IEEE Trans. Robot.*, vol. 33, no. 3, pp. 689–699, Jun. 2017.
[30] F. Karami and Y. Tadesse, "Modeling of twisted and coiled polymer (TCP) muscle based on phenomenological approach," *Smart Mater. Struct.*, vol. 26, no. 12, 2017, Art. no. 125010.
[31] H. Li, L. Liu, T. Xiao, and H. Ang, "Design and simulative experiment of an innovative trailing edge morphing mechanism driven by artificial muscles embedded in skin," *Smart Mater. Struct.*, vol. 25, no. 9, 2016, Art. no. 095004.
[32] L. Sutton, H. Moein, A. Rafiee, J. D. Madden, and C. Menon, "Design of an assistive wrist orthosis using conductive nylon actuators," in *Proc. 6th IEEE Int. Conf. Biomed. Robot. Biomechatronics*, 2016, pp. 1074–1079.
[33] L. Saharan, M. J. de Andrade, W. Saleem, R. H. Baughman, and Y. Tadesse, "igrab: Hand orthosis powered by twisted and coiled polymer muscles," *Smart Mater. Struct.*, vol. 26, no. 10, 2017, Art. no. 105048.
[34] Y. Almubarak and Y. Tadesse, "Twisted and coiled polymer (TCP) muscles embedded in silicone elastomer for use in soft robot," *Int. J. Intell. Robot. Appl.*, vol. 1, no. 3, pp. 352–368, 2017.
[35] A. Abbas and J. Zhao, "A physics based model for twisted and coiled actuator," in *Proc. IEEE Int. Conf. Robot. Autom.*, May 2017, pp. 6121–6126.
[36] Q. Yang and G. Li, "A top-down multi-scale modeling for actuation response of polymeric artificial muscles," *J. Mech. Phys. Solids*, vol. 92, pp. 237–259, 2016.
[37] R. M. Murray, Z. Li, S. S. Sastry, and S. S. Sastry, *A Math. Int. Robotic Manipulation*. Boca Raton, FL, USA: CRC Press, 1994.
[38] D. C. Rucker and R. J. Webster, "Computing jacobians and compliance matrices for externally loaded continuum robots," in *Proc. IEEE Int. Conf. Robot. Autom.*, May 2011, pp. 945–950.
[39] J. L. Sparks *et al.*, "Use of silicone materials to simulate tissue biomechanics as related to deep tissue injury," *Adv. Skin Wound Care*, vol. 28, no. 2, pp. 59–68, 2015.

Benjamin Pawlowski received the B.S. degree in mechanical engineering from Colorado State University, Fort Collins, CO, USA, in 2017. He is currently working toward the M.S. degree in mechanical engineering from Colorado State University.

His research interests include modeling and control of soft robots.

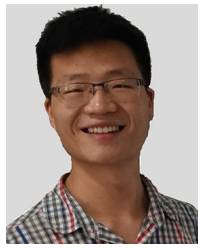

Jiefeng Sun received the B.S. degree in mechanical engineering in 2014 from Lanzhou University of Technology, Lanzhou, China, and the M.E. degree in mechanical engineering in 2017 from Dalian University of Technology, Dalian, China. He is currently working toward the Ph.D. degree in mechanical engineering with Colorado State University, Fort Collins, CO, USA.

His current research interests include artificial muscle and soft robots.

Jing Xu (M'12) received the B.E. degree in mechanical engineering from Harbin Institute of Technology, Harbin, China, in 2003, and the Ph.D. degree in mechanical engineering from Tsinghua University, Beijing, China, in 2008.

He was a Postdoctoral Researcher with the Department of Electrical and Computer Engineering, Michigan State University, East Lansing, MI, USA. He is currently an Associate Professor with the Department of Mechanical Engineering, Tsinghua University, Beijing, China. His research interests include vision-guided manufacturing, image processing, and intelligent robotics.

Yingxiang Liu (M'12–SM'16) received the B.E., M.E., and Ph.D. degrees from the School of Mechatronics Engineering, Harbin Institute of Technology, Harbin, China, in 2005, 2007, and 2011, respectively.

He is currently a Professor with the School of Mechatronics Engineering and a member of the State Key Laboratory of Robotics and System, Harbin Institute of Technology. He was a Visiting Scholar with the Mechanical Engineering Department, University of California, Berkeley, CA, USA, from 2013 to 2014. His research interests include piezoelectric actuating, ultrasonic motors, piezoelectric actuators, precision actuating, piezoelectric micro jets, bionic robots, fish robots, and soft robots.

Dr. Liu has served as an Associate Editor of IEEE ACCESS.

Jianguo Zhao (M'15) received the B.E. degree in mechanical engineering from Harbin Institute of Technology, Harbin, China, and the M.E. degree in mechatronic engineering from Shenzhen Graduate School, Harbin Institute of Technology, Shenzhen, China, in 2005 and 2007, respectively. He received the Ph.D. degree in electrical engineering from Michigan State University, East Lansing, MI, USA, in 2015.

He is currently an Assistant Professor with Colorado State University, Fort Collins, CO, USA. His research interests include bioinspired robotics, dynamics and control, and vision-based control.